AGU PUBLICATIONS

Global Biogeochemical Cycles

RESEARCH ARTICLE
10.1002/2014GB005007

Key Points:
- We present a δ^{13}C-CH_4 record of the rapid CH_4 variation 85ka before present
- We apply Keeling plot analysis and validate the results against a box model
- We propose that tropical wetland emissions caused the observed CH_4 anomaly

Correspondence to:
P. Sperlich,
peter.sperlich@niwa.co.nz

Citation:
Sperlich, P., H. Schaefer, S. E. Mikaloff Fletcher, M. Guillevic, K. Lassey, C. J. Sapart, T. Röckmann, and T. Blunier (2015), Carbon isotope ratios suggest no additional methane from boreal wetlands during the rapid Greenland Interstadial 21.2, *Global Biogeochem. Cycles*, *29*, 1962–1976, doi:10.1002/2014GB005007.

Received 7 OCT 2014
Accepted 27 SEP 2015
Accepted article online 1 OCT 2015
Published online 30 NOV 2015

©2015. American Geophysical Union. All Rights Reserved.

Carbon isotope ratios suggest no additional methane from boreal wetlands during the rapid Greenland Interstadial 21.2

Peter Sperlich[1,2,3], Hinrich Schaefer[3], Sara E. Mikaloff Fletcher[3], Myriam Guillevic[1,4,5], Keith Lassey[3,6], Célia J. Sapart[7,8], Thomas Röckmann[7], and Thomas Blunier[1]

[1]Centre for Ice and Climate, University of Copenhagen, Copenhagen, Denmark, [2]Max-Planck-Institute for Biogeochemistry, Jena, Germany, [3]National Institute of Water and Atmospheric Research, Wellington, New Zealand, [4]Laboratoire des Sciences du Climat et de l'Environnement, Gif sur Yvette, France, [5]Now at Swiss Federal Institute of Metrology, Bern-Wabern, Switzerland, [6]Lassey Research and Education Ltd, Lower Hutt, New Zealand, [7]Institute for Marine and Atmospheric Research Utrecht, Utrecht University, Utrecht, Netherlands, [8]Now at Laboratoire de Glaciologie, Université Libre de Bruxelles, Brussels, Belgium

Abstract Samples from two Greenland ice cores (NEEM and NGRIP) have been measured for methane carbon isotope ratios (δ^{13}C-CH_4) to investigate the CH_4 mixing ratio anomaly during Greenland Interstadial (GI) 21.2 (85,000 years before present). This extraordinarily rapid event occurred within 150 years, comprising a CH_4 mixing ratio pulse of 150 ppb (~25%). Our new measurements disclose a concomitant shift in δ^{13}C-CH_4 of 1‰. Keeling plot analyses reveal the δ^{13}C of the additional CH_4 source constituting the CH_4 anomaly as -56.8 ± 2.8‰, which we confirm by means of a previously published box model. We propose tropical wetlands as the most probable additional CH_4 source during GI-21.2 and present independent evidence that suggests that tropical wetlands in South America and Asia have played a key role. We find no evidence that boreal CH_4 sources, such as permafrost degradation, contributed significantly to the atmospheric CH_4 increase, despite the pronounced warming in the Northern Hemisphere during GI-21.2.

1. Introduction

Methane (CH_4) is a strong greenhouse gas that is accumulating in Earth's atmosphere due to human activity. Currently, CH_4 contributes 20% of the anthropogenic increase in radiative forcing since 1750 [e.g., *Forster et al.*, 2007] and plays a significant role in recent and projected variations of global temperature, sea level, and sea ice extent [e.g., *Meehl et al.*, 2007]. Reconstructions of atmospheric CH_4 mixing ratios (mixing ratios of all gases are indicated by [...] in the following) from ice core samples show distinct variations from decadal [e.g., *Grachev et al.*, 2007; *Chappellaz et al.*, 2013; *Mitchell et al.*, 2013] to orbital timescales [e.g., *Loulergue et al.*, 2008]. Rapid [CH_4] increases of the order of 150–300 ppb occurred over decades to centuries in association with Northern Hemispheric warm events [e.g., *Brook et al.*, 1996; *Grachev et al.*, 2007]. We use the most recent nomenclature after *Rasmussen et al.* [2014] and name the cold periods "Greenland Stadial" (GS) and the intermittent warm events "Greenland Interstadial" (GI).

High-resolution data sets show that some GI events were preceded by sharp precursor events of high amplitude, e.g., GI-21.2 [e.g., *Grachev et al.*, 2007; *Capron et al.*, 2010; *Boch et al.*, 2011; *Vallelonga et al.*, 2012; *Chappellaz et al.*, 2013; *Deplazes et al.*, 2013]. The rapid GI-21.2 event about 85,000 years before 2000 A.D. (b2k) comprised a [CH_4] spike of ~150 ppb that occurred within ~150 years (Figure 1). This extraordinary event is marked by the highest [CH_4] growth rate recorded in Greenland ice cores [*Chappellaz et al.*, 2013]. Rapid [CH_4] changes of this magnitude and timescale are of particular interest for studies on the biogeochemistry of CH_4 and the sensitivity of CH_4 source fluxes to climate change.

Atmospheric chemistry models suggest that the [CH_4] variability during GI events was mostly driven by variations in the sources of CH_4 rather than the sinks [*Levine et al.*, 2012]. Atmospheric CH_4 sources have distinct isotopic compositions in both δ^{13}C and δ^{2}H that depend on the source processes and the CH_4 precursor material [e.g., *Quay et al.*, 1999; *Whiticar and Schaefer*, 2007]. Observations of δ^{13}C-CH_4 or δ^{2}H-CH_4 can therefore constrain CH_4 source flux reconstructions, which can then be interpreted in the context of climate variability [e.g., *Ferretti et al.*, 2005; *Schaefer et al.*, 2006; *Sowers*, 2006; *Fischer et al.*, 2008; *Bock et al.*, 2010; *Sapart et al.*, 2012].

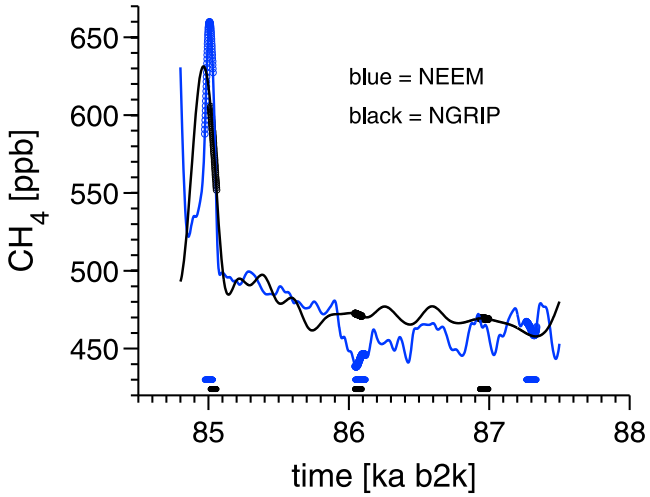

Figure 1. [CH_4] spline fits for NEEM (blue) and NGRIP (black). Circles on the lines and bars at the bottom of the plot highlight the locations of the δ^{13}C-CH_4 samples relative to [CH_4].

Isotope records of CH_4 suggest tropical and/or boreal wetland source flux variations as main drivers of the [CH_4] variability [e.g., *Sowers*, 2006; *Fischer et al.*, 2008; *Mischler et al.*, 2009; *Bock et al.*, 2010; *Möller et al.*, 2013]. Furthermore, isotopic evidence clearly demonstates that CH_4 hydrate destabilization was not the primary CH_4 source that caused the [CH_4] variability during the last deglaciation [*Sowers*, 2006], GI-7 and GI-8 [*Bock et al.*, 2010].

Most studies that analyzed the isotopic variability of CH_4 in ice core samples use mass balance calculations in box models [e.g., *Ferretti et al.*, 2005; *Schaefer et al.*, 2006; *Sowers*, 2006; *Fischer et al.*, 2008; *Mischler et al.*, 2009; *Bock et al.*, 2010; *Sapart et al.*, 2012]. Here we investigate the change in δ^{13}C-CH_4 that is associated with the [CH_4] anomaly of GI-21.2 using Keeling plot analysis (KPA) [*Keeling*, 1958]. KPA is technically a two-component mixing model that provides the δ^{13}C-CH_4 of an additional CH_4 source, which in our case is the source of the [CH_4] anomaly of GI-21.2. We present a Monte Carlo technique that considers both the analytical and data processing errors as well as a potential sampling bias in order to estimate the uncertainty of the KPA. Then, we compare the δ^{13}C-CH_4 result from the KPA to the result from the forward stepping box model of *Lassey et al.* [2007] and show that the two methods agree well within the uncertainty of the KPA.

Recently, *Möller et al.* [2013] suggested that δ^{13}C-CH_4 and [CH_4] vary independently on millennial to glacial-interglacial timescales, which also questions the suitability of mass balance calculations for CH_4 source reconstructions on the timescales of our study period. We therefore test alternative scenarios where the δ^{13}C-CH_4 excursion of GI-21.2 is superimposed on a long-term δ^{13}C-CH_4 trend that is controlled by [CO_2]. We argue that KPA and mass balance calculations can be used in our study period when the effect of possible δ^{13}C-CH_4 background scenarios is carefully considered.

To our knowledge, this is the first time KPA is applied to studies of CH_4 in ice core samples. Therefore, we first review assumptions and necessary conditions for the use of KPA and then explain the processes that need to be considered in order to reconstruct the δ^{13}C of an additional CH_4 source from ice core samples. Finally, we discuss and evaluate CH_4 emission scenarios in the context of other, independent climate records.

2. Methods

2.1. Measurement Techniques

Our analytical technique for δ^{13}C-CH_4 analysis is described in detail by *Sperlich et al.* [2013]. In short, cleaned ice core samples are melted in a vacuum system from which the liberated air sample is extracted. A helium carrier gas stream transports the sample through the analytical system to isolate CH_4 and to combust it into CO_2 before it is measured for δ^{13}C on an isotope ratio mass spectrometer. Our δ^{13}C results are reported on the Vienna Peedee Belemnite isotope scale, using the referencing technique described by *Sperlich et al.* [2012]. The analytical uncertainty of the δ^{13}C-CH_4 measurements is 0.09‰. Our analytical method is free of krypton artifacts which have recently been identified as a major problem in δ^{13}C-CH_4 measurements [*Schmitt et al.*, 2013].

Optical measurement techniques were recently applied to measure [CH_4] in ice core samples [*Stowasser et al.*, 2012] and provided a continuous record of unprecedented temporal resolution and precision from the NEEM ice core [*Chappellaz et al.*, 2013]. This new method presents the [CH_4] of GI-21.2 in unprecedented detail. Discrete [CH_4] measurements from the NGRIP ice core show the anomaly of GI-21.2 in comparable magnitude [*Baumgartner et al.*, 2014]. We fitted two splines to the [CH_4] records from *Chappellaz et al.* [2013] and *Baumgartner et al.* [2014] to calculate the mean [CH_4] of our δ^{13}C-CH_4 samples (Figure 1). The spline of the NEEM data includes a 25 year smoothing filter, while replicate measurements of [CH_4] in the NGRIP record were averaged to avoid artifacts. The NEEM and the NGRIP spline fit show a slightly different timing for GI-21.2. However, timing offsets between the records can be corrected for because [CH_4] varies synchronously in the atmosphere [*Blunier et al.*, 2007]. The higher temporal resolution of the NEEM [CH_4] record justifies to transfer the NGRIP [CH_4] data to the NEEM timescale for GI-21.2. Therefore, we used the NEEM spline in our box model calculations (section 2.6).

2.2. Ice Core Samples for δ^{13}C-CH_4 Measurements

The rapid GI-21.2 event is recorded within only ~1.5 m in the NEEM ice core [*Chappellaz et al.*, 2013]. Because the number of available ice core samples from GI-21.2 and GS-22 is extremely limited (0.55 m ice per sample), we used samples from both the NEEM and NGRIP ice cores for δ^{13}C-CH_4 analysis. We measured four samples of the stadial period preceding GI-21.2 (GI-22), when [CH_4] was stable. We analyzed two samples of GI-21.2 and six younger samples of the strong [CH_4] variation of GI-21.1e (Figure 2). The age interval that is integrated within each of our δ^{13}C-CH_4 samples from GS-22 and GI-21.2 is displayed in relation to the [CH_4] history in Figure 1. Together, our two GI-21.2 samples integrate more than 50% of the event, including the [CH_4] peak and the highest rates of [CH_4] change.

2.3. Applied Corrections on δ^{13}C-CH_4 Measurements

All δ^{13}C-CH_4 measurements are corrected for firn diffusion fractionation after *Buizert et al.* [2013]. This correction depends on the physical properties of the respective gas species, its relative growth rate, and a site-specific time-dependent factor, which is determined by the diffusive column height. The firn diffusion fractionation is generally smaller at Greenlandic than at central Antarctic sites. Our firn diffusion correction reaches maximum values of 0.34‰ during GI-21.2. This semiempirical method is published with a general, relative uncertainty of 30% for Greenland ice cores.

We also correct the δ^{13}C-CH_4 and [CH_4] data for the disequilibrium effect [*Tans*, 1997] that we determined with the box model of *Lassey et al.* [2007]. The disequilibrium effect for both δ^{13}C-CH_4 and [CH_4] is most pronounced for our GI-21.2 samples, where it accounts for up to 0.12‰ and 24 ppb, respectively. We discuss the relevance of this correction on our KPA results in section 3.1.

2.4. Assumptions for the Analysis of δ^{13}C-CH_4 During Greenland Interstadial 21.2 Using Mass Balance Calculations

Because the limited amount of sample ice restricts the temporal data resolution, even our high-resolution record with an average resolution of one sample per 380 years includes a data gap of ~1000 years, just before the onset of the GI-21.2 event. This requires an assumption as to the timing of the δ^{13}C-CH_4 variation before the GI-21.2 event, which is critical for the analysis.

We can think of three different δ^{13}C-CH_4 background scenarios:

1. The variation of δ^{13}C-CH_4 is correlated with [CH_4]; i.e., the δ^{13}C-CH_4 background does not change before the onset of GI-21.2 (Figure 2c). This scenario is in agreement with most of the existing publications on δ^{13}C-CH_4 in ice core samples [e.g., *Ferretti et al.*, 2005; *Schaefer et al.*, 2006; *Sowers*, 2006; *Fischer et al.*, 2008; *Mischler et al.*, 2009; *Bock et al.*, 2010; *Sapart et al.*, 2012]. In particular, *Melton et al.* [2012] recently reported a variation in δ^{13}C-CH_4 in correspondence to a rapid change in [CH_4]. In the following, we will refer to this as the [CH_4]-correlated background scenario.
2. The δ^{13}C-CH_4 is controlled by [CO_2] on millennial to glacial timescales (Figure 2b) as recently published by *Möller et al.* [2013]. We will name this the [CO_2]-correlated background scenario throughout this study.
3. A δ^{13}C-CH_4 depletion that is continuous from the last measured pre-event value to the peak of GI-21.2 (Figure 2a).

Other evolutions of the δ^{13}C-CH_4 background cannot be ruled out but are highly speculative. We reject scenario 3 (as well as other δ^{13}C-CH_4 background histories), because there is no mechanistic explanation for a δ^{13}C-CH_4 variability that is not linked to either [CH_4] or [CO_2].

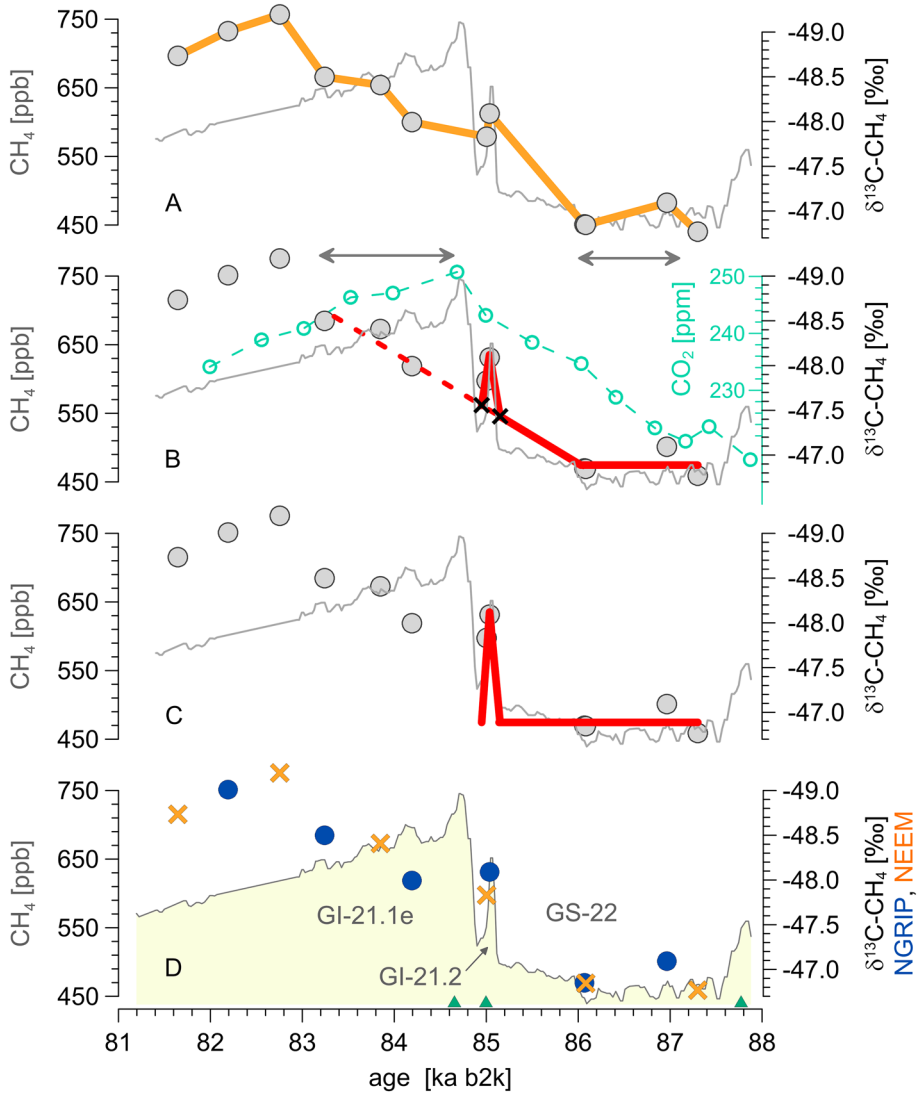

Figure 2. δ^{13}C-CH_4 background scenarios: (left *y* axes) [CH_4], grey lines [*Chappellaz et al.*, 2013]; (right *y* axes) δ^{13}C-CH_4, filled symbols. Figures 2a–2c show the discussed scenarios of the δ^{13}C-CH_4 background during the sample gap between 85–86 ka b2k and the GI-21.2 event. (a) The δ^{13}C-CH_4 as direct (orange) line between measurements. (b) [CO_2] [*Bereiter et al.*, 2012], δ^{13}C-CH_4 reconstruction based on the [CO_2]-correlated background (red line) as determined by the regression (red, dashed line); two arrows indicate the time lag between [CO_2] and δ^{13}C-CH_4 that averages to ~1270 years. (c) δ^{13}C-CH_4 reconstruction based on the [CH_4]-correlated background scenario (red line). (d) The δ^{13}C-CH_4 measurements from NGRIP and NEEM ice cores. Note the good agreement between the 86 ka samples from both ice cores and the ^{13}C enrichment with decreasing [CH_4] at the end of the GI-21.2 event. Green triangles (Figure 2d) indicate points to match [CH_4] from the EPICA Dronning Maud Land (EDML) ice core [*Schilt et al.*, 2010] and NEEM to transfer [CO_2] from the EDML gas age scale to GICC05_modelext [*Blunier et al.*, 2007].

Also, the δ^{13}C-CH_4 peak and decline of GI-21.2 indicate that the δ^{13}C-CH_4 signal is indeed a positive excursion and not just part of a longer-term trend. Changes in [CH_4] indicate variations in CH_4 emissions (assuming no or small sink variability). These necessarily incur changes in δ^{13}C-CH_4 of the total source and consequently the atmosphere, except for the unlikely case that all sources change by the same relative amounts. Therefore, the coinciding excursions in [CH_4] and δ^{13}C-CH_4 can be analyzed for the underlying source changes [*Ferretti et al.*, 2005; *Schaefer et al.*, 2006; *Sowers*, 2006; *Fischer et al.*, 2008; *Mischler et al.*, 2009; *Bock et al.*, 2010; *Sapart et al.*, 2012]. The [CO_2]-correlated δ^{13}C-CH_4 variability [*Möller et al.*, 2013] must also be taken into account. However, this can only explain a part of the GI-21.2 δ^{13}C-CH_4 excursion. A significant δ^{13}C-CH_4 deviation linked to the [CH_4] peak is evident even if superimposed on a longer-term, [CO_2]-correlated trend in δ^{13}C-CH_4 (Figure 2b). Therefore, we hypothesize that scenarios 1 and 2 represent the outer bounds for the possible

evolution of the δ^{13}C-CH_4 background, in agreement with previous publications. The δ^{13}C-CH_4 excursion that is superimposed on the background trends can be analyzed with KPA and mass balance calculations because of its short duration of GI-21.2 and the likelihood of little variability in δ^{13}C-CH_4 background. We present separate solutions for scenarios 1 and 2. Because there is no evidence to prefer either the [CH_4]- or the [CO_2]-correlated background scenario, we use the average of both analyses and their propagate uncertainty.

Furthermore, we argue that our measurements and samples are appropriate to reconstruct the atmospheric variability of GI-21.2. Air is subject to mixing and diffusion processes in the firn column, before air is permanently trapped in the ice [e.g., *Buizert et al.*, 2012], which smoothes the recorded atmospheric signal. Ice core studies are therefore liable to underestimate atmospheric variability. However, previous studies showed excellent agreement between overlapping δ^{13}C-CH_4 measurements in atmospheric, firn-air, and ice core samples [*Francey et al.*, 1999; *Ferretti et al.*, 2005] (note that potential disagreements between multiple δ^{13}C-CH_4 firn-air records are largely based on analytical artifacts and laboratory offsets [*Sapart et al.*, 2013] that may range in the order of 0.5‰ [*Sapart et al.*, 2011]). The ice core samples from *Ferretti et al.* [2005] originated from a high-accumulation site where firn smoothing window is smaller than in central Greenland (≤20 years [*Ferretti et al.*, 2005] versus ≤80 years with mean of ~25 years [*Spahni et al.*, 2003]). Furthermore, the [CH_4] growth rate was significantly larger during the time period studied by *Ferretti et al.* [2005] compared to that of GI-21.2 (5–17 ppb/yr [*Etheridge et al.*, 1998] versus 2.5 ppb/yr [*Chappellaz et al.*, 2013]), where a larger growth rate increases the impact of firn column effects. Therefore, we expect that firn smoothing has a negligible effect on our record. Our two samples of the GI-21.2 event integrate about 50% of the [CH_4] variability (Figure 1), which might dampen the atmospheric signal. Because we average [CH_4] over the exact time period that is integrated in each δ^{13}C-CH_4 sample for the KPA, we expect that the impact of the sample integration on the KPA result is not significant.

It is furthermore important to note that our δ^{13}C-CH_4 samples integrate 40–70 years between sample top and bottom. For the KPA, we use [CH_4] and δ^{13}C-CH_4 of identical ice cores and average [CH_4] over the time period that is integrated in each δ^{13}C-CH_4 sample. Because of this time integration, our analysis resolves variations as 40–70 year averages.

2.5. Keeling Plot Analysis

2.5.1. Keeling Plot Analysis for CH_4 Source Determination in Atmospheric Samples

For the KPA, the isotopic composition of a group of samples is plotted versus its inverse mixing ratio. The intercept of the linear regression with the *y* axis indicates the average isotopic signature of a trace gas source [*Keeling*, 1958]. This technique represents a two-component mixing model with background air and one additional source of analyte gas as the only principal components [*Pataki et al.*, 2003]. *Pataki et al.* [2003] express the global atmospheric budget as

$$c_a = c_b + c_s \tag{1}$$

where c_a, c_b, and c_s represent the CH_4 mixing ratios as measured in the atmosphere, the background atmosphere, and the term due to the additional source, respectively. While c_a and c_b are directly measured, c_s can be calculated after equation (1), because we assume that the background is well defined by the measurements of c_b.

Referring to the isotopic composition of each term by δ^{13}C, the mass balance calculation

$$\delta^{13}C_a c_a = \delta^{13}C_b c_b + \delta^{13}C_s c_s \tag{2}$$

allows to calculate the $\delta^{13}C_s$ of the additional CH_4 source that accounts for c_s in the present-day atmosphere [e.g., *Fisher et al.*, 2011].

2.5.2. Keeling Plot Analysis for CH_4 Source Analysis in Ice Core Samples

Unlike for direct atmospheric measurements (e.g., in the vicinity of CH_4 point sources), KPA on δ^{13}C-CH_4 in ice core samples does not provide the isotopic composition of an additional CH_4 source directly, because two additional mechanisms have to be taken into account. There are the atmospheric disequilibrium effect [e.g., *Tans*, 1997] and the impact of the atmospheric sink fractionation (ε) on the δ^{13}C of the additional CH_4 source. Every ice core measurement needs to be corrected for the average disequilibrium effect per sample, which can be determined with a box model based on measured [CH_4] and δ^{13}C-CH_4 time series, resulting in $\delta^{13}C_{a-corr}$, $\delta^{13}C_{b-corr}$, c_{a-corr}, and c_{b-corr}. Secondly, the $\delta^{13}C_s$ term in equation (2) has been altered by atmospheric sink

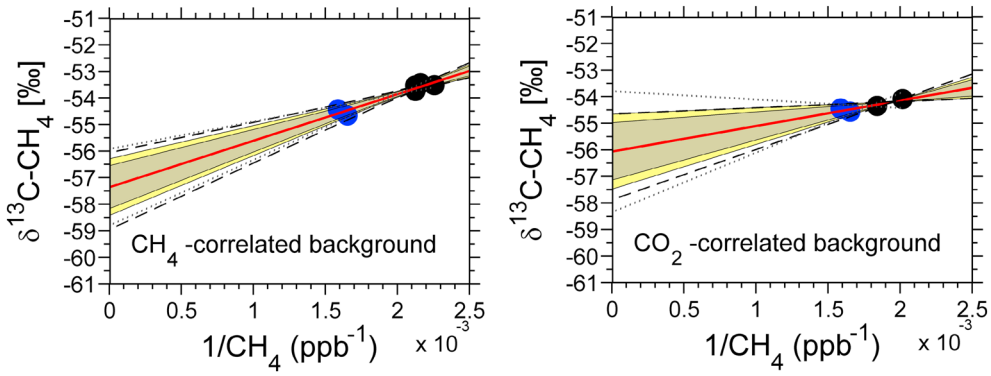

Figure 3. Keeling plots with uncertainties. (left) Keeling Plot with two measurements from GI-21.2 (blue circles) and [CH_4]-correlated background as represented by four measurements from GS-22 (black circles). (right) Keeling Plot of [CO_2]-correlated background, similar to Figure 3 (left) except that the two black circles indicate the two artificial data points. Red lines represent the linear fit; grey and yellow shading illustrate the 95 and 99% confidence intervals of the linear fit as determined by the Monte Carlo analysis, respectively. Dotted lines indicate the least squares uncertainty; dashed lines indicate the uncertainty estimate of the "quasi" bootstrap.

fractionation of a similar magnitude as $\delta^{13}C_a$ and $\delta^{13}C_b$. By solving equation (2) for $\delta^{13}C_s$ and accounting for the disequilibrium effect correction and the sink weighted isotope fractionation (ε_{tot}), we get

$$\delta^{13}C_s = \frac{(\delta^{13}C_{a-corr} \times c_{a-corr} - \delta^{13}C_{b-corr} \times c_{b-corr})}{c_s} \times \left(1 + \frac{\varepsilon_{tot}}{1000}\right) + \varepsilon_{tot} \quad (3)$$

and are able to calculate the $\delta^{13}C$ of the additional CH_4 source in ice core samples.

2.5.3. The Isotopic Fractionation of the Total CH_4 Sink in Keeling Plot Analysis

Literature values of ε_{tot} vary from −7.7‰ [*Lassey et al.*, 2007] to −5.4‰ [*Mischler et al.*, 2009], while it has been suggested to scale ε_{tot} to [CH_4] on glacial-interglacial timescales [*Schaefer and Whiticar*, 2008]. The determination of ε_{tot} depends on the isotope fractionation of the respective CH_4 sinks and their relative contribution to the total sink fluxes. Note that both factors are likely to have varied on glacial-interglacial timescales and that the cumulative effect on ε_{tot} on glacial timescales is not well understood [e.g., *Schaefer and Whiticar*, 2008; *Levine et al.*, 2012]. The weak correlation between [CH_4] and $\delta^{13}C$-CH_4 on millennial to glacial timescales [*Möller et al.*, 2013] further suggests that the forcing of [CH_4] on ε_{tot} is not controlling $\delta^{13}C$-CH_4. We apply the ε_{tot} of −7.0‰ that *Schaefer and Whiticar* [2008] calculated for the preindustrial Holocene and discuss the effect of different ε_{tot} scenarios on our results in section 3.1.

2.5.4. Uncertainty Estimate of Least Squares Fit in Keeling Plot Analysis

A linear regression is used to calculate the slope and intercept of the KPA. This is often undertaken using a least squares fit, where the confidence interval of the fit is calculated based on the uncertainty of both slope and intercept, the degrees of freedom ($n - 2$), and the according quantiles of a Student's t distribution at the chosen confidence level (Figure 3). We see two disadvantages of the least squares uncertainty in our case:

1. It requires homoscedasticity, whereas the residuals of our linear fit show a bimodal distribution of the variance with clusters during the background period (GS-22) and during GI-21.2. The residuals of GI-21.2 data are larger by a factor of 2. Violating the precondition of homogenous variance of the residuals might therefore produce a data-specific bias, which we cannot investigate further because of the limited number of samples.
2. The least squares uncertainty neither considers the analytical uncertainty of 0.09‰ nor the uncertainty of the firn diffusion correction. The latter accounts for 0.11‰ in both GI-21.2 samples and for ≤ 0.01‰ in all samples from GS-22 and GI-21.1e. The combined analytical uncertainty is thus clustered with higher uncertainties during GI-21.2, which is not reflected in the least squares scenario. We address these issues with a Monte Carlo estimate of the uncertainty.

2.5.5. Uncertainty Estimate of Keeling Plot Analysis Using Monte Carlo Technique

We designed a Monte Carlo simulation to determine 95 and 99% confidence intervals for least squares linear regressions based on the propagated uncertainties of each data point. In this approach, we randomly perturbed all data points independently, then performed a regression on the perturbed data, and repeated this process 10,000 times.

We calculated the perturbations as the sum of two perturbations, one based on a Gaussian distribution with a standard deviation equal to the measurement uncertainty (0.09‰) and one with a standard deviation equal to the data point specific uncertainty of the firn diffusion correction (0.01–0.11‰). These two perturbations were calculated independently, such that they might have an additive impact for some iterations and a canceling effect for others. The 95 and 99% confidence intervals were then calculated as the 2.5–97.5 and 0.5–99.5 percentile values of the resulting regression curves. Because we have only two data points from GI-21.2, we constructed a quasi bootstrap method to account for errors from sampling bias. Here the same Monte Carlo routine used the background data of the four GI-22 samples, but it was assigned either one or the other data point of GI-21.2 twice, each time in combination with a new randomized uncertainty. This quasi bootstrap method calculates another two sets of 10,000 regressions for each case, that either of our two GI-21.2 samples represents the true value better than both values together. We show the 95 and 99% confidence intervals of the complete data set and furthermore the uppermost and lowermost 99% confidence interval boundaries of the quasi bootstrap in Figure 3. Note that the range between the latter two compares well to the uncertainties of the least squares method (section 2.5.4). We consider the Monte Carlo approach to be the more robust uncertainty estimate for several reasons: (1) It enables to calculate 95 and 99% of the linear fits that can all be seen as best scenarios within the uncertainty of our data. Therefore, it provides valuable, structural information of the uncertainty range. (2) It is free of assumptions regarding the distribution of the residuals. (3) The quasi bootstrap method quantifies the sampling bias.

2.5.6. Determining the [CO_2]-Correlated δ^{13}C-CH_4 Background Scenario for Keeling Plot Analysis of GI-21.2

Möller et al. [2013] show the surprisingly strong correlation between δ^{13}C-CH_4 and [CO_2] during the last 160 ka and highlight periods when the correlation seems to break down, including the period after the onset of GI-21.1. The latter occurs during the 2300 year data gap in their record between 80.3 and 82.6 ka b2k Before the sample at 82.6 ka b2k, i.e., during our study period, δ^{13}C-CH_4 and [CO_2] seem to correlate [*Möller et al.*, 2013, Figure 1]. However, the average temporal resolution of 1660 years in this part of the record from *Möller et al.* [2013] complicates the precise timing of the correlation breakdown. Our data of this period are of higher temporal resolution and show a correlation between the δ^{13}C-CH_4 background and [CO_2] during GS-22 and the early part of GI-21.1e, if we allow for an average time lag between [CO_2] and δ^{13}C-CH_4 of ~1270 years (Figure 2b). Interestingly, this time lag is in agreement with *Burckel et al.* [2015], who found that changes in the Atlantic Meridional Overturning Circulation (AMOC) preceded precipitation changes in tropical South America during the last glacial period by 500–1700 years. This could provide an additional mechanistic clue to the correlation between [CO_2] and δ^{13}C-CH_4 as interpreted by *Möller et al.* [2013], as the AMOC is related to changes in atmospheric [CO_2] [*Bereiter et al.*, 2012] and the precipitation in South America to tropical CH_4 emissions, where the latter impact δ^{13}C-CH_4 (Table 2). Note that independently of a precise determination of the time lag, the correlation between δ^{13}C-CH_4 and [CO_2] during the period just before and after GI-21.2 is evident. Therefore, the assumption of the [CO_2]-correlated background scenario with monotonous δ^{13}C-CH_4 depletion around GI-21.2 is justified.

In order to determine the [CO_2]-correlated δ^{13}C-CH_4 background scenario, we use three of our measurements from GI-21.1e that are ≤2000 years younger than GI-21.2. We fitted a regression through these three data points from GI-21.1e and the latest two measurements of GS-22 (red dashed line in Figure 2b). The resulting [CO_2]-correlated background scenario for GI-21.2 and GS-22 is indicated by the thick red line in Figure 2b. Then, we calculated the δ^{13}C-CH_4 in two points from just before and just after GI-21.2 based on the regression (black crosses in Figure 2b) and determined the corresponding [CH_4] data from *Chappellaz et al.* [2013] (Table 1). The two generated data pairs simulate a hypothetical background scenario for the case that the [CO_2]-correlated trend in δ^{13}C-CH_4 represents the atmospheric δ^{13}C-CH_4 variation around GI-21.2 more accurately than the [CH_4]-correlated background (thick red line in Figure 2c). A KPA was then performed using the two artificial data points as background and our measured data from GI-21.2. This experiment highlights two important results: (1) GI-21.2 shows a significant δ^{13}C-CH_4 event even when superimposed on a long-term δ^{13}C-CH_4 trend (Table 1). (2) Using both background scenarios for KPA leads to similar CH_4 source signatures that agree within the uncertainty estimate (Figure 3). In this study, the backgound assumption does not impact on our interpretation of the KPA result.

2.6. Configuration of a Box Model to Test Results From Keeling Plot Analysis

We configured the box model of *Lassey et al.* [2007] so that a base source and an additional source can be implemented in order to compare KPA and box model outputs. Specifically, the KPA assumes that atmosphere,

Table 1. δ^{13}C-CH_4 and [CH_4] Data Used for Keeling Plot Analysis[a]

Ice Core	Age(ka b2k)	δ^{13}C-CH_4(‰)	[CH_4](ppb)
NEEM	85.003	−47.83	635
NGRIP	85.036	−48.12	581
NGRIP	86.068	−46.85	472
NEEM	86.083	−46.84	444
NGRIP	86.964	−47.09	469
NEEM	87.301	−46.77	463
—	84.950	−47.56[b]	553[c]
—	85.150	−47.43[b]	496[c]

[a]Columns 1–4 show sample site, mean gas age on the GICC05 time scale [*Wolff et al.*, 2010]. δ^{13}C-CH_4 after correction for firn diffusion fractionation, and mean [CH_4] per δ^{13}C-CH_4 sample, respectively.
[b]Artificial δ^{13}C-CH_4 values for [CO_2]-correlated background (Figure 2b).
[c][CH_4] values for [CO_2]-correlated background from *Chappellaz et al.* [2013].

sources, and sink are in equilibrium, whereas the box model accounts for disequilibrium effects as discussed by *Tans* [1997]. The CH_4 source flux in the box model is set to reconstruct a smoothed spline fit (25 year smoothing window) of the NEEM [CH_4] record from *Chappellaz et al.* [2013] (Figure 4a). The background source is configured to simulate the atmospheric [CH_4] history during GS-22 by varying the source fluxes of background CH_4 while a constant δ^{13}C is assigned (Figure 4d). The δ^{13}C of background CH_4 was estimated as −53.6‰ by averaging the δ^{13}C-CH_4 of our samples from GS-22 and correcting them for ε_{tot} of −7.0‰ (equation (3)). The onset of the GI-21.2 event occurs in the year 85,100 b2k in our [CH_4] spline fit. The box model is configured to use a constant flux of the background source (fixed at the 85,100 b2k value) thereafter and to match the atmospheric [CH_4] history of GI-21.2 by varying the flux of the additional CH_4 source (Figure 4e) with a δ^{13}C-CH_4 that can be varied. The δ^{13}C-CH_4 value of the additional source is chosen so that the atmospheric δ^{13}C-CH_4 history is in best agreement with our two δ^{13}C-CH_4 measurements from GI-21.2 (red circles in Figure 4e). We defined best agreement such that the difference to the modeled δ^{13}C-CH_4 history is identical for both of our δ^{13}C-CH_4 samples. The box model solves for the δ^{13}C of the additional CH_4 during GI-21.2, which we compare to the δ^{13}C-CH_4 result of the KPA. We also apply the δ^{13}C-CH_4 background of the [CO_2]-correlated scenario in a box model run to compare the results to the KPA.

In addition, the box model is used to estimate the disequilibrium effect that results from changes in CH_4 source fluxes and the δ^{13}C of CH_4 sources [*Tans*, 1997]. The impact of the disequilibrium effect on δ^{13}C scales with ε_{tot}, where a stronger sink fractionation causes a stronger disequilibrium. The disequilibrium effect variation during GS-22 and GI-21.2 is shown in Figures 4b and 4c. It is used to correct both the δ^{13}C and the mean [CH_4] of our δ^{13}C-CH_4 samples for the KPA (equation (3)) and has a small impact on our KPA result.

3. Results

3.1. Results From Keeling Plot Analysis

Our δ^{13}C-CH_4 measurements, the corresponding [CH_4] data, and the two pairs of artificial data for the [CO_2]-correlated background scenario are shown in Table 1. The KPA with [CH_4]-correlated δ^{13}C-CH_4 background intersects the *y* axis at −57.4‰ (Figure 3, left). We derive a conservative uncertainty estimate of ±2‰ from the 99% interval of the quasi bootstrap technique (section 2.5.5). The KPA for the [CO_2]-correlated background scenario intersects the *y* axis at −56.1±2‰ (Figure 3, right). The difference between the two KPA results is 1.3‰, which is well within the uncertainty. The good agreement between KPA using both background scenarios suggests that the assumption regarding the background variation of δ^{13}C-CH_4 during GS-22 is not critical for our interpretation of the results.

Applying the ε_{tot} of −5.4‰ from *Mischler et al.* [2009] to our analysis would shift the KPA results by 1.5‰ toward more enriched δ^{13}C values. Scaling ε_{tot} to [CH_4] due to changes in the soil sink flux as suggested by *Schaefer and Whiticar* [2008] would result in an ε_{tot} for GS-22 and GI-21.2 of −5.9‰ and −6.5‰, respectively, if all other sink fluxes and ε values remained constant. This would increase the difference in δ^{13}C between the

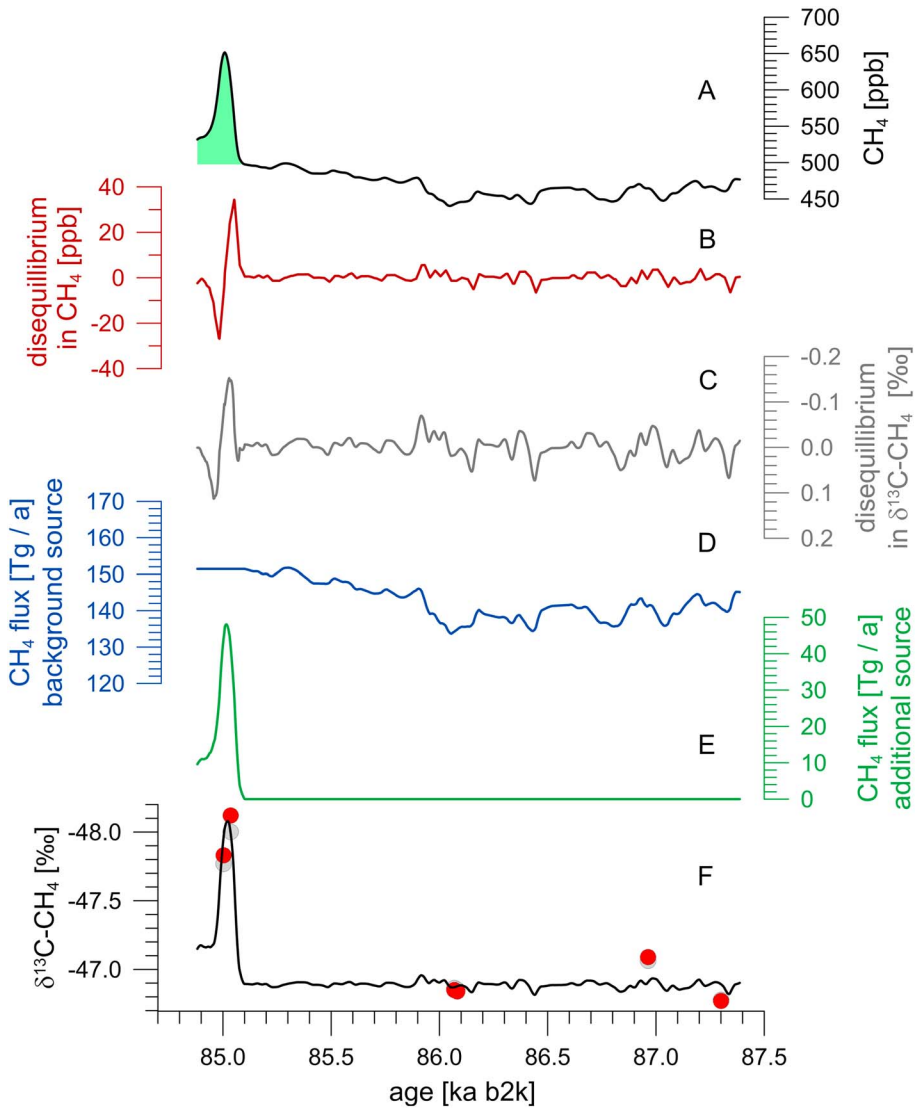

Figure 4. Box model data. (a) The [CH_4] input data [*Chappellaz et al.*, 2013] with GI-21.2 highlighted in green. (b and c) The calculated disequilibrium effect for [CH_4] and δ^{13}C-CH_4, respectively. (d and e) The calculated CH_4 fluxes of the background source and the additional source during GI-21.2, respectively. (f) The δ^{13}C-CH_4 output from the box model in comparison to our δ^{13}C-CH_4 measurements before (red circles) and after (grey circles) the disequilibrium correction.

ε_{tot}-corrected GS-22 and GI-21.2 data by 0.6‰ and shift the δ^{13}C of the total sources toward more enriched values. The scaled ε_{tot} scenario would deplete the KPA results by 1.3‰. Note that none of these ε_{tot} scenarios would change our KPA results beyond the uncertainty envelope of ±2‰ and would therefore not change our interpretation of the results.

Applying the disequilibrium correction (equation (3)) shifts the KPA results by 0.4‰ toward stronger δ^{13}C enrichment, which is a small effect compared to the KPA uncertainty of ±2‰.

3.2. Comparing the Results From Keeling Plot Analysis and Box Model

The box model resulted in a δ^{13}C of the additional source that is 0.6‰ more depleted in δ^{13}C than the KPA result of the [CH_4]-correlated δ^{13}C-CH_4 background. For the [CO_2]-correlated background scenario, the box model result is 0.4‰ more enriched in δ^{13}C. The difference between KPA and box model results is of different sign for both scenarios but well within the ±2‰ uncertainty of the KPA. The disagreement between KPA and box model is partly due to the different methods used to determine the mathematical solution. While the KPA result is determined by a least squares fit that considers all data points from GI-21.2 and GS-22, the box model result depends on an equal mismatch between the modeled δ^{13}C-CH_4 scenario and the two GI-21.2 data

Table 2. Average δ^{13}C Isotope Ratios of Categorized CH_4 Sources[a]

Source	δ^{13}C-CH_4 (‰)
Tropical wetlands	−58[b]
Boreal wetlands	−63[b]
CH_4 hydrates	−62.5[b]
Aerobic C3	−58[c]
Aerobic C4	−50[c]
Termites	−70[d]
Geological	−40[e]
Biomass burning	−25[d]
Thermokarst lakes	−70[f]

[a]The data represent average values with an uncertainty of 2–5‰ [e.g., *Quay et al.*, 1999] or even larger for CH_4 hydrates [e.g., *Kvenvolden*, 1995].
[b]From *Whiticar and Schaefer* [2007] for glacial periods.
[c]From *Keppler et al.* [2006].
[d]From *Mikaloff Fletcher et al.* [2004].
[e]From *Denman et al.* [2007].
[f]From *Walter et al.* [2008].

points. Furthermore, the $[CH_4]$ at the beginning of the GI-21.2 event is ∼20 ppb higher than the mean $[CH_4]$ of the background samples from GS-22. To compensate this larger proportion of δ^{13}C-enriched background CH_4 in the box model, the δ^{13}C of the additional CH_4 has to be more depleted. Note that this is not the case for the box model test with the $[CO_2]$-correlated background, which may explain the change of sign in the difference.

3.3. Averaging the Keeling Plot Analyses Results of Both Background Assumptions for Interpretation

For our interpretation, we average the KPA results using the $[CH_4]$- and the $[CO_2]$-correlated background scenarios to −56.8±2.8‰. The averaged result considers both background scenarios as equally possible solutions within the propagated uncertainty range.

4. Discussion

4.1. Applicability of Keeling Plot Analysis to Study the Variation of δ^{13}C-CH_4 in Ice Core Samples

We use KPA for the analyis of δ^{13}C-CH_4 in ice core samples and derive results that agree with a forward stepping box model within the uncertainty of the KPA. For most accurate results, the KPA requires the disequilibrium correction, which can be calculated using a suitable box model in addition to the KPA. However, the disequilibrium correction did not change our KPA results significantly. The disequilibrium effect could be relatively small in our analysis because each of our δ^{13}C-CH_4 samples averages a large part of the GI-21.2 event; hence, extreme values of the disequilibrium effect are smoothed out. This could be different for the analysis of samples with a similar but longer-lasting $[CH_4]$ gradient or samples that integrate a shorter period of time. However, the $[CH_4]$ growth rate during GI.21.2 is to date the highest observed for natural $[CH_4]$ variability [*Chappellaz et al.*, 2013]. Therefore, it seems unlikely that the disequilibrium effect will have a significant impact on a KPA that is performed on other ice core samples during other periods of time.

Besides the fact that KPA can serve as a fast approach for δ^{13}C-CH_4 analysis, it has the advantage over a box model that it is independent of a gas age scale, as KPA only requires the combination of CH_4 and δ^{13}C-CH_4 data. This avoids uncertainties from dating issues that may arise when data sets from more than one ice core are merged for analysis.

4.2. CH_4 Source Identification From Keeling Plot Analysis Result

Our averaged KPA result of −56.8±2.8‰ is in best agreement with the δ^{13}C that *Whiticar and Schaefer* [2007] reconstructed for CH_4 emissions from tropical wetlands during the glacial period (Table 2). Note that aerobic formation of CH_4 in C3 plants is a theoretical solution; however, the process and its relevance are not well understood and can therefore not be discussed in the context of rapid climate changes.

Our preferred solution is that tropical wetland emissions were the most important contributors to the $[CH_4]$ anomaly of GI-21.2. This result is supported by *Baumgartner et al.* [2014], who found that high growth rates, as reported for GI-21.2 [*Chappellaz et al.*, 2013], are associated with an Intertropical Convergence Zone (ITCZ) position that enhances CH_4 emissions from tropical Asia. Another method to constrain the spatial distribution of CH_4 emissions is the relative Inter-Polar Difference (rIPD) of CH_4 [e.g., *Chappellaz et al.*, 1997; *Brook et al.*, 2000; *Baumgartner et al.*, 2014], which is strongly influenced by solar insolation [e.g., *Baumgartner et al.*, 2014]. Because no rIPD reconstruction exists specifically for GI-21.2, we assume that the rIPD of the directly following GI-21.1e is indicative for GI-21.2. This assumption is justified by a maximum insolation gradient between 30°N and 60°N during both GI-21.1e and GI-21.2, with higher insolation in the lower latitudes [*Laskar et al.*, 2004].

The rIPD during GI-21.1e appears to be of medium amplitude with ~7.5%, which indicates the dominance of tropical Northern Hemisphere CH_4 sources [*Baumgartner et al.*, 2014].

Predominant contributions from ^{13}C-depleted CH_4 sources like boreal wetlands would have to be compensated by emissions from ^{13}C-enriched CH_4 sources (such as pyrogenic CH_4) to match the isotope budget. Such a scenario cannot be ruled out by our data but is not consistent with the geographic constraints for the additional CH_4 emissions described above. The KPA precludes either biomass burning or termites as main CH_4 source for the GI-21.2 anomaly (Table 2). Interestingly, an outstanding CH_4 emission pulse from geological mantle sources can also be ruled out, as this CH_4 source is significantly more enriched in ^{13}C [e.g., *Etiope and Lollar*, 2013]. The wide $\delta^{13}C$ range of marine hydrate-bound CH_4 between −57 and −73‰ [e.g., *Kvenvolden*, 1995] with the additional potential for postemission enrichment by microbial oxidation in the water column [e.g., *Whiticar and Faber*, 1986] does not rule out CH_4 hydrate destabilization as the cause of the [CH_4] anomaly during GI-21.2.

To investigate this further, we calculate a Rayleigh distillation as described by *Schaefer et al.* [2006] and find a theoretical CH_4 hydrate emission scenario in which ~47% of released CH_4 is oxidized in sediment and water column while the remaining ~53% reach the atmosphere in agreement with our KPA result. However, this partitioning between CH_4 oxidation and release to the atmosphere is in strong disagreement with the observations of *Yvon-Lewis et al.* [2011], who show that only 0.01% of the CH_4 that was released during the "Deep Water Horizon" spill arrived in the atmosphere. Based on δ^2H-CH_4 data, *Sowers* [2006] and *Bock et al.* [2010] proved that marine hydrate destabilization did not cause the [CH_4] increase during the last deglaciation and of GI-7 and GI-8, respectively. For the above mentioned reasons, we assume that it is unlikely that CH_4 released from marine hydrates has caused the [CH_4] variability during GI-21.2.

In general, it is important to remember that the complex biogeochemistry of natural CH_4 sources leads to wide $\delta^{13}C$ ranges within each source category, thereby limiting the constraining power of $\delta^{13}C$-CH_4 reconstructions. In the following, we compare our hypothesis that mostly tropical CH_4 sources have caused the [CH_4] anomaly during GI-21.2 to independent evidence.

5. Comparison to Independent Climate Records

The strong temperature variability as recorded in Greenland ice cores during the last glacial (e.g., *NGRIP community members* [2004] and Figure 5c) is associated with changes in both atmospheric and ocean circulation [e.g., *Chiang and Friedman*, 2012]. Variations in both are of hemispheric extent and are related to the location of the ITCZ [*Chiang and Friedman*, 2012; *Burckel et al.*, 2015]. The ITCZ location is critical for the regulation of monsoon system intensities by controlling the meridional transport of heat and moisture [*Chiang and Friedman*, 2012; *Burckel et al.*, 2015], which are the main controlling measures of CH_4 emissions [*Guo et al.*, 2012]. Thus, the ITCZ location determines the meridional distribution of CH_4 source regions and thereby the partitioning of CH_4 emissions from the Northern and Southern Hemispheres [e.g., *Guo et al.*, 2012; *Baumgartner et al.*, 2014]. In the following, we discuss the variation of climate proxies in a geographical context in order to test our hypothesis that the CH_4 excursion during GI-21.2 was predominantly caused by increased CH_4 emissions from tropical wetlands.

5.1. South American Monsoon Systems During Greenland Interstadial 21.2

Wang et al. [2004], *Cruz et al.* [2005], and *Deplazes et al.* [2013] reconstruct large-scale precipitation variations in South American rainforest systems: During GS-22, the Atlantic rainforest section of southern South America experienced a wet interval [*Wang et al.*, 2004; *Cruz et al.*, 2005] (Figure 5e), thereby enhancing CH_4 emissions from this region in the Southern Hemisphere. At the same time, marine sediment reflectivity records from the Cariaco Basin indicate that the climate in the much larger Amazonian rainforest system was in a dryer phase [*Deplazes et al.*, 2013] (Figure 5d), which can be expected to reduce CH_4 emissions from the Amazonian region. After GS-22, the large-scale precipitation pattern over South America changed significantly, most likely driven by solar insolation and changes in ocean circulation [*Wang et al.*, 2004; *Burckel et al.*, 2015]. The transition between the two states is resolved in both the Caricao Basin sediments [*Deplazes et al.*, 2013] and the subtropical speleothem records from south Brazil [*Cruz et al.*, 2005], where both records indicate a wetter climate period in the Amazonian rainforest systems during GI-21.2 (Figures 5d and 5e). *Deplazes et al.* [2013] propose a strong precipitation increase in the Amazonian rainforest that coincided with the temperature and [CH_4] anomaly of GI-21.2, thereby linking Greenlandic and South American climate. The ITCZ controlled precipitation pattern in South America [*Wang et al.*, 2004; *Cruz et al.*, 2005; *Deplazes et al.*, 2013] may result in a change

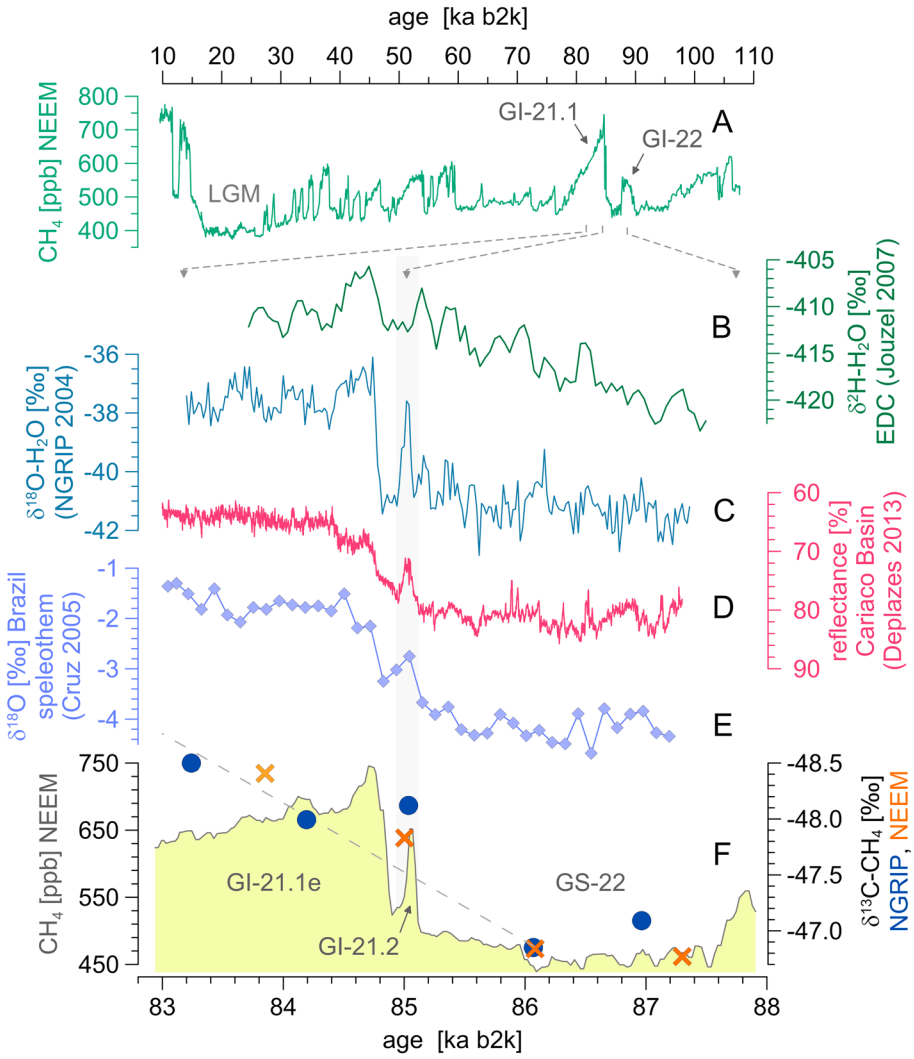

Figure 5. δ^{13}C-CH_4 in comparison to independent climate data. (a) [CH_4] during last glacial [*Chappellaz et al.*, 2013] on the top *x* axis. Figures 5b–5f refer to the bottom *x* axis. The grey bar highlights the GI-21.2 event. (b) Antarctic and (c) Greenlandic water isotope ratios (*Jouzel et al.* [2007] and *NGRIP* [2004], respectively). (d) Reflectivity record of Cariaco Basin [*Deplazes et al.*, 2013] and (e) δ^{18}O from south Brazilian speleothems [*Cruz et al.*, 2005]. (f) Left axis [CH_4] and right axis (inverted) δ^{13}C-CH_4 from NGRIP (circles) and NEEM (crosses). All data are shown on the GICC05_modelext timescale [*Wolff et al.*, 2010]. δ^{18}O Figure 5e is adjusted by +0.55ka to align GI-21.2, which is in line with *Cruz et al.* [2005].

of the dominant South American CH_4 source regions from the smaller Atlantic to the much larger Amazonian region between GS-22 and GI-21.2, possibly triggering CH_4 fluxes from Amazonian wetland sources to cause the [CH_4] anomaly of GI-21.2.

5.2. Asian Monsoon Systems During Greenland Interstadial 21.2

Pausata et al. [2011], *Deplazes et al.* [2013], and *Mohtadi et al.* [2014] propose a teleconnection pattern where North Atlantic cold periods coincided with dryer conditions in the tropical Indian monsoon realm, mediated by changes in atmospheric circulation. Speleothem records of *Wang et al.* [2001, 2008] provide geological evidence that link Greenland climate with the transport of heat and moisture in the distant East Asian monsoon region. A further geological argument for a tight coupling between Greenland temperature and the Asian monsoon system is suggested by *Ruth et al.* [2007], according to which the lower dust concentration observed in Greenland ice cores during GI-21.2 [e.g., *Rasmussen et al.*, 2014] indicates an intensification of the Asian monsoon system. The above mentioned studies suggest warmer and wetter climate in the Asian monsoon region during GI-21.2, where both factors potentially raise tropical wetland CH_4 emissions [e.g., *Brook et al.*, 1996; *Guo et al.*, 2012].

Acknowledgments
We thank everyone involved in logistics, field work, and ice core processing and analysis in the laboratories and during the field campaigns at NEEM and NGRIP. We would also like to thank Willi A. Brand and Martin Heimann for insightful discussions on CH_4 isotopes and KPA as well as the two anonymous reviewers and the Editor for their valuable comments. We acknowledge the availability of data we used for our analysis and Figures. The [CH_4] (NEEM) reconstructions were provided by Thomas Blunier (blunier@nbi.ku.dk). All other data were obtained from the following sources: $\delta^{18}O$ (NGRIP): World Data Center for Paleoclimatology and NOAA Paleoclimatology Program (ftp://ftp.ncdc.noaa.gov/pub/data/paleo/icecore/greenland/summit/ngrip/isotopes/ngrip-d18o-50yr.txt); δ^2H (EDC): NOAA national climatic data center (http://www.ncdc.noaa.gov/paleo/pubs/jouzel2007/jouzel2007.html); CO_2 (EDML): NOAA national climatic data center (ftp://ftp.ncdc.noaa.gov/pub/data/paleo/icecore/antarctica/edml-talos2012co2.txt); CH_4 (EDML): World Data Center for Paleoclimatology and NOAA Paleoclimatology Program (ftp://ftp.ncdc.noaa.gov/pub/data/paleo/icecore/antarctica/maud/edml-ch4-140k.txt); Marine sediment reflectance (Cariaco Basin): Pangaea, (http://doi.pangaea.de/10.1594/PANGAEA.815882); and $\delta^{18}O$ (speleothems): World Data Center for Paleoclimatology and NOAA Paleoclimatology Program (ftp://ftp.ncdc.noaa.gov/pub/data/paleo/speleothem/southamerica/brazil/botuvera2005.txt). This work is a contribution to the NGRIP ice core project, which is directed and organized by the Ice and Climate Research Group at the Niels Bohr Institute, University of Copenhagen. It is being supported by funding agencies in Denmark (SNF), Belgium (FNRS-CFB), France (IPEV, INSU/CNRS and ANR NEEM), Germany (AWI), Iceland (RannIs), Japan (MEXT), Sweden (SPRS), Switzerland (SNF), and the U.S. (NSF). NEEM is directed and organized by the Centre of Ice and Climate at the Niels Bohr Institute and U.S. NSF, Office of Polar Programs. It is supported by funding agencies and institutions in Belgium (FNRS-CFB and FWO), Canada (NRCan/GSC), China (CAS), Denmark (FI), France (IPEV, CNRS/INSU, CEA, and ANR), Germany (AWI), Iceland (RannIs), Japan (NIPR), South Korea (KOPRI), the Netherlands (NWO/ALW), Sweden (VR), Switzerland (SNF), the United Kingdom (NERC), and the U.S. (U.S. NSF, Office of Polar Programs). The research leading to these results has received funding from the European

5.3. Potential for Boreal and Pyrogenic CH_4 Emissions During Greenland Interstadial 21.2

Guo et al. [2012] describe that enhanced monsoon system strength (sections 5.1 and 5.2) increases the meridional transport of heat and moisture into the extratropics, thereby strengthening boreal CH_4 emissions. Also, high Northern Hemisphere summer insolation [*Laskar et al.*, 2004] and the relatively warm polar temperatures [*EPICA*, 2006] during GI-21.2 had the potential to enhance CH_4 emissions from boreal wetlands [e.g., *Brook et al.*, 1996]. However, the CH_4 of boreal wetland sources is relatively depleted in ^{13}C and ranges around −63‰ (Table 2). Moreover, *McCalley et al.* [2014] report a further, systematic $\delta^{13}C$ depletion of CH_4 emissions from newly degrading permafrost soils, which we cannot rule out during the rapid Northern Hemisphere warming of GI-21.2 [*NGRIP*, 2004]. Therefore, our result of −56.8±2.8‰ precludes boreal wetland emissions as the predominant CH_4 source causing the [CH_4] anomaly of GI-21.2 (Table 2). Increased boreal CH_4 emissions would have to be compensated by ^{13}C-enriched pyrogenic CH_4 emissions (−25‰) during the period integrated per $\delta^{13}C$-CH_4 sample to match our reconstructed $\delta^{13}C$-CH_4. *Daniau et al.* [2007] analyzed charcoal records and found increased wildfire intensity in Europe during interstadial periods of the last glacial period, which would be consistent with this scenario.

On the contrary, charcoal records from lower latitudes suggest minimum wildfire intensities during our study period [e.g., *Bird and Cali*, 1998; *Wang et al.*, 2005; *Kershaw et al.*, 2007]. Given that *Thonicke et al.* [2005] report a consistent latitudinal pattern of highest charcoal counts and pyrogenic CH_4 emissions in the lower latitudes and found that this pattern was more pronounced during the LGM, the lack of evidence for increased tropical burning during our study period suggests that global pyrogenic CH_4 formation was small. Consequently, CH_4 emissions from boreal wetland sources must have been small as well to meet the $\delta^{13}C$-CH_4 constraint. This finding strengthens our interpretation that tropical wetlands were the most important CH_4 sources that caused the [CH_4] anomaly of GI-21.2.

6. Conclusions

We present an approach to use Keeling plot analysis to investigate the variability of CH_4 sources in ice core samples, based on $\delta^{13}C$-CH_4 and [CH_4] measurements during GI-21.2. Our Keeling plot analysis includes a correction for the disequilibrium effect, based on information from a time stepping box model. The result of the Keeling plot analysis agrees with the box model results within 0.6‰, which is well within the uncertainty of the Keeling plot analysis (±2‰) for either of the background scenarios.

The average $\delta^{13}C$-CH_4 of the source causing the rapid [CH_4] variability is best matched by enhanced CH_4 emissions from tropical wetlands. Our conclusion is supported by a range of independent climate records, which suggest wetter and warmer climate in tropical Amazonian and Asian CH_4 source ecosystems. Increases in both boreal wetlands and biomass burning were only possible if their relative contributions produced the $\delta^{13}C$ of CH_4 sources suggested by the KPA. Because charcoal records from lower latitudes suggest that the wildfire intensity during our study period was low, a strong response of boreal CH_4 sources to the rapid GI-21.2 event seems unlikely. The hypothesis that boreal CH_4 sources showed a low sensitivity to the short but rapid temperature increase of GI-21.2 [e.g., *NGRIP*, 2004; *Capron et al.*, 2010; *Boch et al.*, 2011] is an interesting finding in the light of global warming and the associated potential for CH_4 emissions from boreal sources such as permafrost (note that GI-21.2 is not a complete analogue for present-day climate conditions). Further research including climate-vegetation modeling and atmospheric observations at highest spatiotemporal resolution is needed to provide reliable scenarios of vegetation dynamics and related changes in isotope ratios of CH_4 emissions in order to fully exploit the information provided by CH_4 isotope records from ice cores.

References

Baumgartner, M., et al. (2014), NGRIP CH_4 concentration from 120 to 10 kyr before present and its relation to a $\delta^{15}N$ temperature reconstruction from the same ice core, *Clim. Past*, *10*, 903–920.

Bereiter, B., D. Lüthi, M. Siegrist, S. Schüpbach, T. F. Stocker, and H. Fischer (2012), Mode change of millennial CO_2 variability during the last glacial cycle associated with a bipolar marine carbon seesaw, *Proc. Natl. Acad. Sci. U.S.A.*, *109*(25), 9755–9760.

Bird, M. I., and J. A. Cali (1998), A million-year record of fire in sub-Saharan Africa, *Nature*, *394*, 767–769.

Blunier, T., R. Spahni, J. M. Barnola, J. Chappellaz, L. Loulergue, and J. Schwander (2007), Synchronization of ice core records via atmospheric gases, *Clim. Past*, *3*(2), 325–330.

Boch, R., H. Cheng, C. Spotl, R. L. Edwards, X. Wang, and P. Hauselmann (2011), NALPS: A precisely dated European climate record 120–60 ka, *Clim. Past*, *7*(4), 1247–1259.

Bock, M., J. Schmitt, L. Möller, R. Spahni, T. Blunier, and H. Fischer (2010), Hydrogen isotopes preclude marine hydrate CH_4 emissions at the onset of Dansgaard-Oeschger events, *Science*, *328*(5986), 1686–1689.

Union's Seventh Framework programme (FP7/2007-2013) under grant agreement 243908, "Past4Future. Climate change—Learning from the past climate". Support for H.S., S,M,F, and in part for P.S. was provided by NIWA under the Climate and Atmosphere Research Programmes CAAC1504 and CAGE1501 (2014/15 SCI).

Brook, E. J., T. Sowers, and J. Orchardo (1996), Rapid variations in atmospheric methane concentration during the past 110,000 years, *Science*, *273*(5278), 1087–1091.

Brook, E. J., S. Harder, J. Severinghaus, E. J. Steig, and C. M. Sucher (2000), On the origin and timing of rapid changes in atmospheric methane during the last glacial period, *Global Biogeochem. Cycles*, *14*(2), 559–572.

Buizert, C., et al. (2012), Gas transport in firn: Multiple-tracer characterisation and model intercomparison for NEEM, Northern Greenland, *Atmos. Chem. Phys.*, *12*(9), 4259–4277.

Buizert, C., T. Sowers, and T. Blunier (2013), Assessment of diffusive isotopic fractionation in polar firn, and application to ice core trace gas records, *Earth Planet. Sci. Lett.*, *361*, 110–119.

Burckel, P., C. Waelbroeck, J. M. Gherardi, S. Pichat, H. Arz, J. Lippold, T. Dokken, and F. Thil (2015), Atlantic Ocean circulation changes preceded millennial tropical South America rainfall events during the last glacial, *Geophys. Res. Lett.*, *42*, 411–418.

Capron, E., et al. (2010), Millennial and sub-millennial scale climatic variations recorded in polar ice cores over the last glacial period, *Clim. Past*, *6*(3), 345–365.

Chappellaz, J., T. Blunier, S. Kints, A. Dällenbach, J. M. Barnola, J. Schwander, D. Raynaud, and B. Stauffer (1997), Changes in the atmospheric CH_4 gradient between Greenland and Antarctica during the Holocene, *J. Geophys. Res. Atmos.*, *102*(D13), 15987–15997.

Chappellaz, J., et al. (2013), High-resolution glacial and deglacial record of atmospheric methane by continuous-flow and laser spectrometer analysis along the NEEM ice core, *Clim. Past*, *9*, 2579–2593.

Chiang, J. C., and A. R. Friedman (2012), Extratropical cooling, interhemispheric thermal gradients, and tropical climate change, *Annu. Rev. Earth Pl. Sc.*, *40*, 383–412.

Cruz, F. W., S. J. Burns, I. Karmann, W. D. Sharp, M. Vuille, A. O. Cardoso, J. A. Ferrari, P. L. S. Dias, and O. Viana (2005), Insolation-driven changes in atmospheric circulation over the past 116,000 years in subtropical Brazil, *Nature*, *434*(7029), 63–66.

Daniau, A. L., M. F. Sanchez-Goni, L. Beaufort, F. Laggoun-Defarge, M. F. Loutre, and J. Duprat (2007), Dansgaard-Oeschger climatic variability revealed by fire emissions in southwestern Iberia, *Quat. Sci. Rev.*, *26*, 1369–1383.

Denman, K. L., et al. (2007), Couplings between changes in the climate system and biogeochemistry, in *Climate Change 2007: The Physical Science Basis. Contribution of Working Group I to the Fourth Assessment Report of the Intergovernmental Panel on Climate Change*, edited by S. Solomon et al., pp. 499–587, Cambridge Univ. Press, Cambridge, U. K., and New York.

Deplazes, G., et al. (2013), Links between tropical rainfall and North Atlantic climate during the last glacial period, *Nat. Geosci.*, *6*(3), 213–217.

EPICA community members (2006), One-to-one coupling of glacial climate variability in Greenland and Antarctica, *Nature*, *444*(7116), 195–198.

Etheridge, D. M., L. P. Steele, R. J. Francey, and R. L. Langenfelds (1998), Atmospheric methane between 1000 A.D. and present: Evidence of anthropogenic emissions and climatic variability, *J. Geophys. Res.*, *103*(D13), 15,979–15,993.

Etiope, G., and B. S. Lollar (2013), Abiotic methane on Earth, *Rev. Geophys.*, *51*(2), 276–299.

Ferretti, D. F., et al. (2005), Unexpected changes to the global methane budget over the past 2000 years, *Science*, *309*(5741), 1714–1717.

Fischer, H., et al. (2008), Changing boreal methane sources and constant biomass burning during the last termination, *Nature*, *452*(7189), 864–867.

Fisher, R. E., et al. (2011), Arctic methane sources: Isotopic evidence for atmospheric inputs, *Geophys. Res. Lett.*, *38*, L21803, doi:10.1029/2011GL049319.

Forster, P., et al. (2007), Changes in atmospheric constituents and in radiative forcing, in *Climate Change 2007: The Physical Science Basis. Contribution of Working Group I to the Fourth Assessment Report of the Intergovernmental Panel on Climate Change*, edited by S. Solomon et al., pp. 129–234, Cambridge Univ. Press, Cambridge, U. K., and New York.

Francey, R. J., M. R. Manning, C. E. Allison, S. A. Coram, D. M. Etheridge, R. L. Langenfelds, D. C. Lowe, and L. P. Steele (1999), A history of $\delta^{13}C$ in atmospheric CH_4 from the Cape Grim Air Archive and Antarctic firn air, *J. Geophys. Res. Atmos.*, *104*(D19), 23,631–23,643.

Grachev, A. M., E. J. Brook, and J. P. Severinghaus (2007), Abrupt changes in atmospheric methane at the MIS 5b-5a transition, *Geophys. Res. Lett.*, *34*, L20703, doi:10.1029/2007GL029799.

Guo, Z. T., X. Zhou, and H. B. Wu (2012), Glacial-interglacial water cycle, global monsoon and atmospheric methane changes, *Clim. Dynam.*, *39*(5), 1073–1092.

Jouzel, J., et al. (2007), Orbital and millennial Antarctic climate variability over the past 800,000 years, *Science*, *317*(5839), 793–796.

Keeling, C. D. (1958), The concentration and isotopic abundances of atmospheric carbon dioxide in rural areas, *Geochim. Cosmochim. Ac.*, *13*, 322–334.

Keppler, F., J. T. G. Hamilton, M. Brass, and T. Röckmann (2006), Methane emissions from terrestrial plants under aerobic conditions, *Nature*, *439*(7073), 187–191.

Kershaw, P. A., S. C. Bretherton, and S. van der Kaars (2007), A complete pollen record of the last 230 ka from Lynch's Crater, north-eastern Australia, *Palaeogeogr. Palaeocl.*, *251*, 23–45.

Kvenvolden, K. A. (1995), A review of the geochemistry of methane in natural gas hydrate, *Org. Geochem.*, *23*, 997–1008.

Laskar, J., P. Robutel, F. Joutel, M. Gastineau, A. C. M. Correia, and B. Levrard (2004), A long-term numerical solution for the insolation quantities of the Earth, *Astron. Astrophys.*, *428*, 261–285.

Lassey, K. R., D. M. Etheridge, D. C. Lowe, A. M. Smith, and D. F. Ferretti (2007), Centennial evolution of the atmospheric methane budget: What do the carbon isotopes tell us?, *Atmos. Chem. Phys.*, *7*, 2119–2139.

Levine, J. G., E. W. Wolff, P. O. Hopcroft, and P. J. Valdes (2012), Controls on the tropospheric oxidizing capacity during an idealized Dansgaard-Oeschger event, and their implications for the rapid rises in atmospheric methane during the last glacial period, *Geophys. Res. Lett.*, *39*, L12805, doi:10.1029/2012GL051866.

Loulergue, L., A. Schilt, R. Spahni, V. Masson-Delmotte, T. Blunier, B. Lemieux, J. M. Barnola, D. Raynaud, T. F. Stocker, and J. Chappellaz (2008), Orbital and millennial-scale features of atmospheric CH_4 over the past 800,000 years, *Nature*, *453*(7193), 383–386.

McCalley, C. K., B. J. Woodcroft, S. B. Hodgkins, R. A. Wehr, E.-H. Kim, R. Mondav, P. M. Crill, J. P. Chanton, V. I. Rich, G. W. Tyson, and S. R. Saleska (2014), Methane dynamics regulated by microbial community response to permafrost thaw, *Nature*, *453*(7193), 383–386.

Meehl, G. A., et al. (2007), Couplings between changes in the climate system and biogeochemistry, in *Climate Change 2007: The Physical Science Basis. Contribution of Working Group I to the Fourth Assessment Report of the Intergovernmental Panel on Climate Change*, edited by S. Solomon et al., pp. 499–587, Cambridge Univ. Press, Cambridge, U. K., and New York.

Melton, J. R., H. Schaefer, and M. J. Whiticar (2012), Enrichment in $\delta^{13}C$ of atmospheric CH_4 during the Younger Dryas termination, *Clim. Past*, *8*, 1177–1197.

Mikaloff Fletcher, S. E., P. P. Tans, L. M. Bruhwiler, J. B. Miller, and M. Heimann (2004), CH_4 sources estimated from atmospheric observations of CH_4 and its $^{13}C/^{12}C$ isotopic ratios: 1. Inverse modeling of source processes, *Global Biogeochem. Cycles*, *18*, GB4004, doi:10.1029/2004GB002223.

Mischler, J. A., T. A. Sowers, R. B. Alley, R. B. M. Battle, J. R. McConnell, L. Mitchell, T. Popp, E. Sofen, and M. K. Spencer (2009), Carbon and hydrogen isotopic composition of methane over the last 1000 years, *Global Biogeochem. Cycles*, *23*, Gb4024, doi:10.1029/2009GB003460.

Mitchell, L., E. Brook, J. E. Lee, C. Buizert, and T. Sowers (2013), Constraints on the Late Holocene anthropogenic contribution to the atmospheric methane budget, *Science*, *342*(6161), 964–966.

Mohtadi, M., M. Prange, D. W. Oppo, R. De Pol-Holz, U. Merkel, X. Zhang, S. Steinke, and A. Lückge (2014), North Atlantic forcing of tropical Indian Ocean climate, *Nature*, *509*, 76–80.

Möller, L., T. Sowers, M. Bock, R. Spahni, M. Behrens, J. Schmitt, H. Miller, and H. Fischer (2013), Independent variations of CH_4 emissions and isotopic composition over the past 160,000 years, *Nat. Geosci.*, *6*(10), 885–890.

NGRIP community members (2004), High-resolution record of Northern Hemisphere climate extending into the last interglacial period, *Nature*, *431*(7005), 147–151.

Pataki, D. E., J. R. Ehleringer, L. B. Flanagan, D. Yakir, D. R. Bowling, C. J. Still, N. Buchmann, J. O. Kaplan, and J. A. Berry (2003), The application and interpretation of Keeling plots in terrestrial carbon cycle research, *Global Biogeochem. Cycles*, *17*(1), 1022, doi:10.1029/2001GB001850.

Pausata, F. S. R., D. S. Battisti, K. H. Nisancioglu, and C. M. Bitz (2011), Chinese stalagmite $\delta^{18}O$ controlled by changes in the Indian monsoon during a simulated Heinrich event, *Nat. Geosci.*, *4*(7), 474–480.

Quay, P., J. Stutsman, D. Wilbur, A. Snover, E. Dlugokencky, and T. Brown (1999), The isotopic composition of atmospheric methane, *Global Biogeochem. Cycles*, *13*(2), 445–461.

Rasmussen, S. O., et al. (2014), A stratigraphic framework for abrupt climatic changes during the last glacial period based on three synchronized Greenland ice-core records: Refining and extending the INTIMATE event stratigraphy, *Quat. Sci. Rev.*, *106*, 14–28.

Ruth, U., M. Bigler, R. Röthlisberger, M. L. Siggaard-Andersen, S. Kipfstuhl, K. Goto-Azuma, M. E. Hansson, S. J. Johnsen, H. Y. Lu, and J. P. Steffensen (2007), Ice core evidence for a very tight link between North Atlantic and east Asian glacial climate, *Geophys. Res. Lett.*, *34*, L03706, doi:10.1029/2006GL027876.

Sapart, C. J., et al. (2011), Simultaneous stable isotope analysis of methane and nitrous oxide on ice core samples, *Atmos. Meas. Tech.*, *4*(12), 2607–2618.

Sapart, C. J., et al. (2012), Natural and anthropogenic variations in methane sources during the past two millennia, *Nature*, *490*(7418), 85–88.

Sapart, C. J., et al. (2013), Can the carbon isotopic composition of methane be reconstructed from multi-site firn air measurements?, *Atmos. Chem. Phys.*, *13*(14), 6993–7005.

Schaefer, H., and M. J. Whiticar (2008), Potential glacial-interglacial changes in stable carbon isotope ratios of methane sources and sink fractionation, *Global Biogeochem. Cycles*, *22*, GB1001, doi:10.1029/2006GB002889.

Schaefer, H., M. J. Whiticar, E. J. Brook, V. V. Petrenko, D. F. Ferretti, and J. P. Severinghaus (2006), Ice record of $\delta^{13}C$ for atmospheric CH_4 across the Younger Dryas-Preboreal transition, *Science*, *313*(5790), 1109–1112.

Schilt, A., et al. (2010), Atmospheric nitrous oxide during the last 140,000 years, *Earth Planet. Sci. Lett.*, *300*, 33–43.

Schmitt, J., B. Seth, M. Bock, H. Fischer, L. Möller, C. J. Sapart, M. Prokopiou, C. Van der Veen, T. Röckmann, and T. Sowers (2013), On the interference of Kr during carbon isotope analysis of atmospheric methane using continuous flow combustion—Isotope ratio mass spectrometry, *Atmos. Meas. Tech.*, *6*, 1425–1445.

Sowers, T. (2006), Late quaternary atmospheric CH_4 isotope record suggests marine clathrates are stable, *Science*, *311*(5762), 838–840.

Spahni, R., J. Schwander, J. Flückiger, B. Stauffer, J. Chappellaz, and D. Raynaud (2003), The Attenuation of Fast Atmospheric CH_4 Variations Recorded in Polar Ice Cores, *Geophys. Res. Lett.*, *30*(11), 1571, doi:10.1029/2003GL017093.

Sperlich, P., M. Guillevic, C. Buizert, T. M. Jenk, C. J. Sapart, H. Schaefer, T. J. Popp, and T. Blunier (2012), A combustion setup to precisely reference $\delta^{13}C$ and $\delta^{2}H$ isotope ratios of pure CH_4 to produce isotope reference gases of $\delta^{13}C$-CH_4 in synthetic air, *Atmos. Meas. Tech.*, *5*(9), 2227–2236.

Sperlich, P., C. Buizert, T. M. Jenk, C. J. Sapart, M. Prokopiou, T. Röckmann, and T. Blunier (2013), An automated GC-C-GC-IRMS setup to measure paleoatmospheric $\delta^{13}C$-CH_4, $\delta^{15}N$-N_2 and $\delta^{18}O$-N_2O in one ice core sample, *Atmos. Meas. Tech.*, *6*(8), 2027–2041.

Stowasser, C., et al. (2012), Continuous measurements of methane mixing ratios from ice cores, *Atmos. Meas. Tech.*, *5*(5), 999–1013.

Tans, P. P. (1997), A note on isotopic ratios and the global atmospheric methane budget, *Global Biogeochem. Cycles*, *11*(1), 77–81.

Thonicke, K., C. I. Prentice, and C. Hewitt (2005), Modeling glacial-interglacial changes in global fire regimes and trace gas emissions, *Global Biogeochem. Cycles*, *19*, GB3008, doi:10.1029/2004GB002278.

Vallelonga, P., et al. (2012), Duration of Greenland Stadial 22 and ice-gas Delta age from counting of annual layers in Greenland NGRIP ice core, *Clim. Past*, *8*(6), 1839–1847.

Walter, K. M., J. P. Chanton, F. S. Chapin, E. A. G. Schuur, and S. A. Zimov (2008), Methane production and bubble emissions from Arctic lakes: Isotopic implications for source pathways and ages, *J. Geophys. Res. Biogeo.*, *113*, G00a08, doi:10.1029/2007JG000569.

Wang, X., P. A. Peng, and Z. L. Ding (2005), Black carbon records in Chinese Loess Plateau over the last two glacial cycles and implications for paleofires, *Palaeogeogr. Palaeocl.*, *223*, 9–19.

Wang, X. F., A. S. Auler, R. L. Edwards, H. Cheng, P. S. Cristalli, P. L. Smart, D. A. Richards, and C. C. Shen (2004), Wet periods in northeastern Brazil over the past 210 kyr linked to distant climate anomalies, *Nature*, *432*(7018), 740–743.

Wang, Y. J., H. Cheng, R. L. Edwards, Z. S. An, J. Y. Wu, C. C. Shen, and J. A. Dorale (2001), A high-resolution absolute-dated Late Pleistocene monsoon record from Hulu Cave, China, *Science*, *294*(5550), 2345–2348.

Wang, Y. J., H. Cheng, R. L. Edwards, X. G. Kong, X. H. Shao, S. T. Chen, J. Y. Wu, X. Y. Jiang, X. F. Wang, and Z. S. An (2008), Millennial- and orbital-scale changes in the East Asian monsoon over the past 224,000 years, *Nature*, *451*(7182), 1090–1093.

Whiticar, M., and E. Faber (1986), Methane oxidation in sediment and water column environments—Isotopic evidence, *Org. Geochem.*, *10*, 759–768.

Whiticar, M., and H. Schaefer (2007), Constraining past global tropospheric methane budgets with carbon and hydrogen isotope ratios in ice, *Philos. Trans. R. Soc. A*, *365*(1856), 1793–1828.

Wolff, E. W., J. Chappellaz, T. Blunier, S. O. Rasmussen, and A. Svensson (2010), Millennial-scale variability during the last glacial: The ice core record, *Quat. Sci. Rev.*, *29*, 2828–2838.

Yvon-Lewis, S. A., L. Hu, and J. Kessler (2011), Methane flux to the atmosphere from the Deepwater Horizon oil disaster, *Geophys. Res. Lett.*, *38*, 10.1029/2010GL045928.